# Rubin Observatory Simonyi Survey Telescope Active Optics

Sandrine Thomas, Andrew Connolly, John Franklin Crenshaw, Kalmbach J. Bryce, Guillem Megias, Joshua E. Meyers, Tiago Ribeiro, Te-Wei Tsai, Chuck Claver, Doug Neill, et al.

AO4ELT7 - June 2023 - Avignon

# Rubin Observatory Simonyi Survey Telescope Active Optics

Sandrine J. Thomas[a], Andrew Connolly[b], John Franklin Crenshaw[a], J. Bryce Kalmbach[b], Guillem Megias[c], Joshua E. Meyers[c], Tiago Ribeiro[a], Krzysztof Suberlak[b], Te-Wei Tsai[a], Chuck Claver[a], Doug Neill[a], Vittorio F. Braga[d], Giuliana Fiorentino[d], Salvatore Savarese[d], Pietro Schipani[d], Laura Schreiber[d], and Marcella Di Criscienzo[d]

[a]Vera C. Rubin Observatory
[b]University of Washington
[c]SLAC, Stanford Linear Accelerator Center
[d]INAF

## ABSTRACT

The Vera C. Rubin Observatory's Simonyi Survey Telescope (Simonyi Telescope) is an 8.4m telescope now in the integration and testing phase, on Cerro Pachon in Chile. To fulfill the Rubin Observatory scientific objectives of conducting a decade-long time domain survey of the optical sky, the Legacy Survey of Space and Time (LSST) [4], the telescope requires delivering a consistent exquisite image quality over its 3.5 degrees field of view (FoV). This is accomplished using a sophisticated active optics system (AOS). In addition to correct the predictable static and gravity induced aberrations in open-loop, there are four curvature wavefront sensors (CWFs) at the periphery of the detector. These CFWs allow to calculate, in quasi-real time (40s), the appropriate correction offsets to be sent to the three Simonyi Telescope's actuated mirrors and the two hexapods, to further improve the image quality. In this paper, we describe the algorithms optimization and trade-offs, including the use of PSF moments variations for telescope alignment as well as wavefront error estimation. To validate these studies in advance of on-sky testing, we are using both a simulation tool and our 1.2m Auxiliary Telescope equipped with a subset of identical hardware and software as the Simonyi Telescope. Finally, we will describe our on on-sky testing strategy.

**Keywords:** Vera C. Rubin, LSST, telescope, Survey

Further author information: (Send correspondence to Sandrine J. Thomas)
Sandrine J. Thomas: E-mail: sthomas@lsst.org

## 1. SIMONYI SURVEY TELESCOPE'S ACTIVE OPTICS OVERVIEW

The Vera C. Rubin Observatory (Rubin Obs hereafter) has now entered the integration and testing phase on Cerro Pachón in Chile. This ground-based facility is designed to conduct the Legacy Survey of Space and Time (LSST), which is a decade-long time-domain optical survey of the night sky [4]. The scientific requirements of the observatory require the telescope to have an optical system that would deliver an image quality better than 0.4".

The Rubin Observatory optical system utilizes a compact, three-mirror design consisting of an 8.4-meter primary mirror (M1 [2]), 3.4-meter secondary mirror (M2 [7]), and a 5.0-meter tertiary mirror (M3 [2]). This system feeds a large three-lens refractive corrector (camera) that produces a well-corrected 3.5 degree field-of-view. The tertiary mirror resides within the 5-meter diameter central hole of the primary mirror and the two mirrors (M1M3) share the same cast borosilicate substrate, to improve the stiffness and reduce control degrees of freedom. Since the position of the M3 with the M1 is not adjustable, it simplifies optical alignment and enables a compact, rigid structural packaging design. An active optics system (AOS) will optimize the image quality by controlling the surface figures of the mirrors and maintaining the needed alignment between the optical subsystems (M1M3, M2, and camera).

The alignment between each optical component is done at the beginning of each night, to ensure that the residual wavefront error is within the capture range of the wavefront sensors. A laser tracker located at the center of the M1M3 mirror measures the position of M2 and the camera relative to M1M3 using retroreflectors located at the edge of each optical elements (see Figure 1-left). The position adjustments of M2 and the camera are made using the M2 and Camera hexapods. More information on the status of the optical elements can be found in Thomas et al. [13].

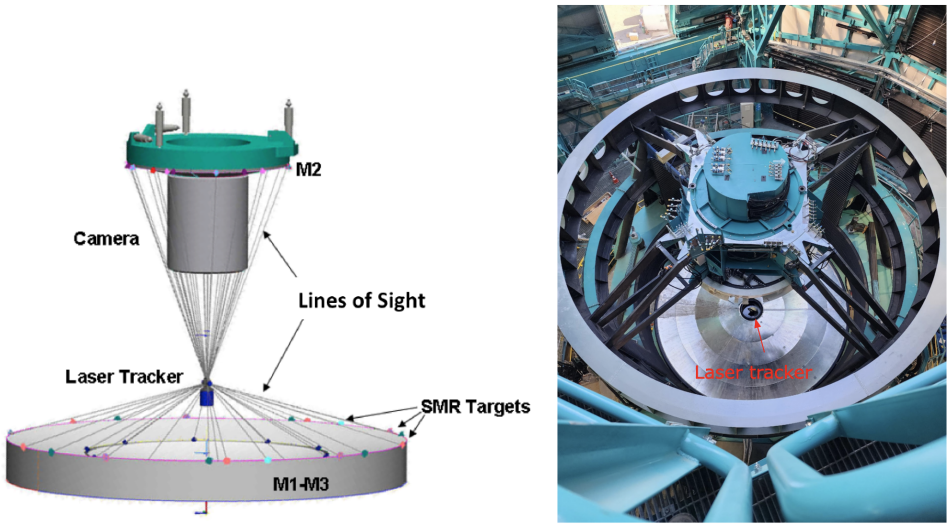


Figure 1. Left: position diagram of the reflectors on the different optical elements. The bottom circle represents the retroreflectors positioned at the periphery of M1M3, the top circle are the ones positioned on M2 and the middle ones on the camera. The goal is to ensure each circles are parallel and their centers are aligned. Right: Laser Tracker installed on the Telescope Mount Assembly, and being tested.

The Active Optics Systems (AOS) is designed to optimize the image quality by controlling the surface figures of the mirrors and maintaining the relative position of the three optical systems (M1M3 mirror, M2 mirror and the camera). Due to the required image quality, the system needs to not only correct for the gravity induced errors but also the errors due to temperature variations, hysteresis, and any other unexpected system errors. Therefore, the Rubin Observatory AOS consists of two control components:

(1) Open-Loop Component (or Look-Up-Table LUT): Most telescopes have an AOS to compensate for intrinsic aberrations of each mirror, gravity induced flexure, and in some instance to control for temperature induced

figure or alignment changes. This is done by using an open-loop model created from a Finite Element Analysis (FEA) model and validated on sky.

(2) Real-time closed-loop Component: the LSST's requirements on resolution and depth pushes the AOS to add a real time feedback control in addition to compensate for temperature effects and hysteresis. This is done using wavefront sensors on the periphery of the detector and sending offsets to the open-loop model (LUT). Each of the 4 wavefront sensors is a pair of defocused half-sensors (see Figure 2) in order to use curvature wavefront sensing algorithms. This is called the baseline mode.

In addition to using these wavefront sensors, there is the possibility to defocus the entire detector on both side of the focal plane using the camera hexapod, which is called the **full-array mode**. Two exposures (one intra focal and one extra focal) will then be needed.

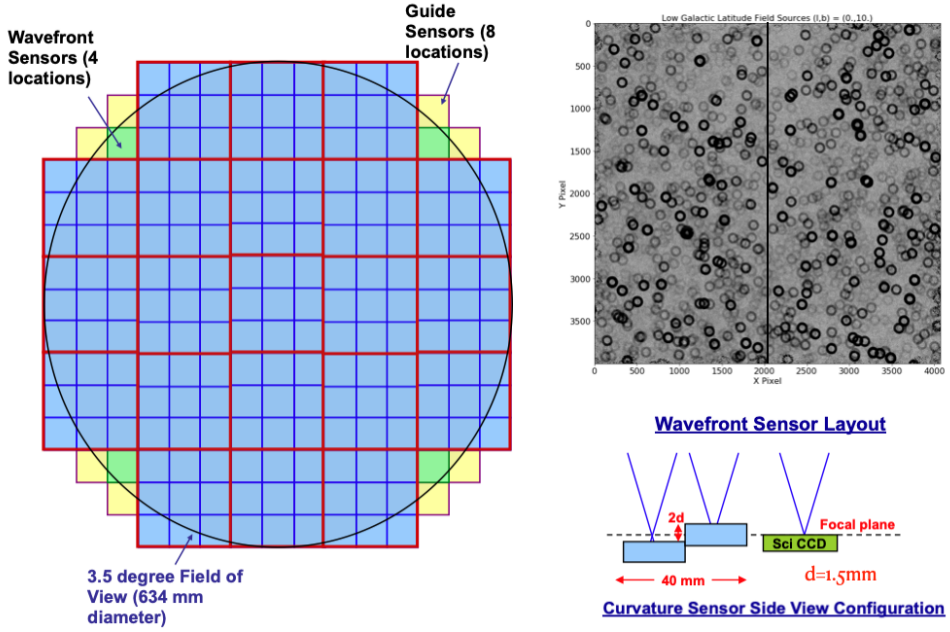


Figure 2. Focal plane configuration for the LSST Camera (left panel) showing sensors used for science (blue), guiding (yellow), and wavefront sensing (green), and side view of the wavefront sensor layout with two example half-chip images (right panel).

For both modes, the wavefront sensing method used is curvature sensing [9] and uses defocused images of stars to derive the wavefront error. More details about the wavefront sensing itself and its challenges for Rubin Observatory can be found in Ref. [15].

In order to actively correct any wavefront errors, each mirror is equipped with actuators in addition to the degrees of freedom of both hexapods.

- M1M3 support system: During observing, the M1M3 mirror is actively supported by 156 pneumatic figure control actuators and 6 bigger actuators called hardpoints, defining the mirror's position. These figure control actuators resist loads (gravitational, wind, dynamic, etc) and provide the active optics figure control. When the active system is not operating, the mirror is supported by a separate passive support system consisting of wire rope isolators. Because the M1M3 mirror is made out of borosilicate, it is quite sensitive to temperature inhomogeneities. This effect is mitigated by a complex thermal control system that uses approximately 90 glycol/water supplied and air blower assemblies to supply temperature controlled air.
- M2 support system:

The 72 electromechanical figure control actuators are used to support the glass mirror in the optical axis direction, and actively control the shape of its optical surface. A separate tangent link system is used to provide transverse support. Because of the low thermal expansion coefficient of the Ultra Low Expansion (ULE), the M2 mirror does not require thermal control.

- M2 and Camera Hexapods: The M2 mirror system and the camera are supported by hexapods to allow for position adjustments. The M2 and camera hexapods will also be principally operated by an open loop LUT system which is a function of elevation angle and bulk temperature change. They must also accommodate refocus during a filter change. Wavefront offsets to the open-loop model are provided by the closed-loop system.

In this paper, we focus on the closed-loop aspect of the Rubin Observatory active optics.

### 1.1 Wavefront Sensing: Curvature WFS

The focal plane of the detector has 189 science sensors, 4 wavefront sensors and 8 guide sensors. Because of their location, the wavefront sensors will have some vignetting and distortion effects that need to be taken into account in the wavefront estimation. Each wavefront sensor consists of two 2K×4K sensors permanently defocused relative to the focal plane, creating images of stars defocused into donuts as shown on Figure 2. This mode is called the **baseline mode**. Another way to obtain the images of defocused donuts required for wavefront sensing is to move the entire detector on both side of the focal plane using the camera hexapod. This mode is called the **full-array mode**.

### 1.2 Algorithm Architecture

Once the images are acquired, they are available for the Main Telescope Active Optics System (MTAOS) control software to process. The Wavefront Estimation Pipeline (WEP) analyzes the donuts and calculates the wavefront error at each of the detectors' locations as Zernike coefficients. Then the wavefront errors are combined by the Optical Feedback Controller (OFC) to estimate the best correction that needs to be sent to the different actuators that control the different degrees of freedom (M1M3, M2 and both the camera and M2 hexapods).

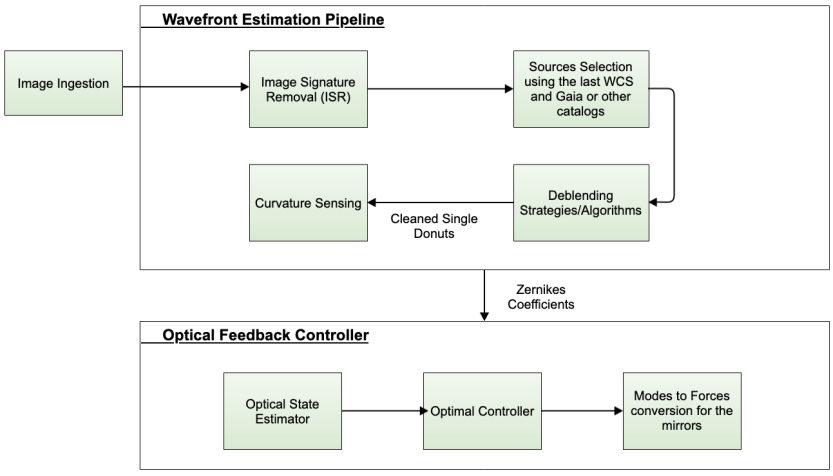


Figure 3. This graphs details the main components of the closed loop pipeline, from images to correction offsets. The main two elements are the wavefront estimation pipeline (WEP) and the Optical Feedback Controller (OFC)

As mentioned above, the wavefront sensing method chosen is the curvature wavefront sensing, adapted to the optical configuration of the Rubin Simonyi Survey Telescope; the large central obstruction (60%), the fast F/number (f/1.23), the off-axis distortion and vignetting, and the field dependent correction. Previous papers have dealt with a number of these constraints [15, 12]. At this stage, the closed-loop code is been tested using

simulated isolated donuts from low to high density fields. The baseline is meeting the image quality error budget allocated for the AOS. The simulations tools used in the context are PhoSim [8] and ImSim [6] *.

### 1.3 Donut Data Processing

Contrary to images obtained generally for adaptive optics for which only an on axis bright single star is used, the active optics raw images have multiple donuts, often blended together, depending on the density of the fields observed (see Figure 4). In addition, the extra-focal and intra-focal images are at different locations and consequently have different stars on them.

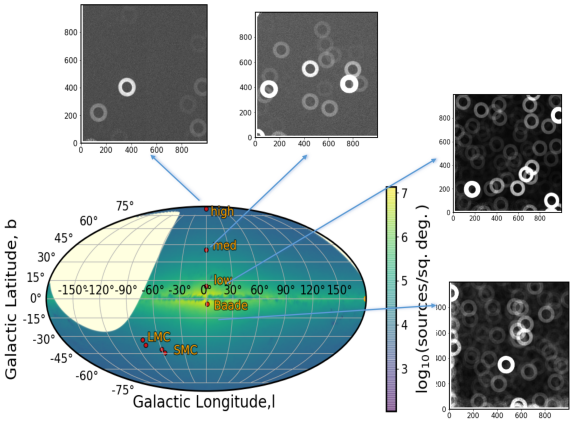


Figure 4. Example of field density and overlapping donut depending on field position. Note that the color scale is not the same on all the images.

As a result, several steps of data processing are needed before the regular curvature wavefront sensing can be applied using one or several donuts from each of the wavefront sensors. At least one donut per detector is required to apply the curvature sensing algorithm.

First, a regular image signature removal process is used to correct for typical errors such as biases and darks. Then catalogs such as Gaia, Pan-Starr and eventually Rubin, are used to pre-select candidate stars that will be used in the curvarure sensing step. The selection process uses a success criteria based on the following attributes: magnitude of the targets, field position of the targets (for vignetting), separation from neighboring sources, magnitude difference between neighbors, number of blended neighbors, and amount of overlap of blended neighbors (for validity of deblending algorithm). The final source catalog is sorted by source brightness and the needed number of targets per iteration is optimized, taking into account Signal to Noise Ratio (SNR) and time needed for the calculation. Figure 5,right, shows example of potential images of different magnitudes. The SNR has to be sufficiently high to limit any noise propagation in the correction. This can be done by either choosing only bright targets or by adding results from different pairs of, even faint, donuts.

Once the best donuts are selected on each side of the wavefront sensor detector using the process above, the baseline is to apply the curvature sensing measurement on pairs of 2 donuts from each chip of a corner raft [12]. We are exploring the stacking of donuts from each chip to get two "master" donuts, however we find that it is not computationally useful as it does not seem to improve performances to the expense of time.

### 1.4 Handling Vignetting

Because the wavefront sensors are located at the periphery of the focal plane, some of the detectors are subject to vignetting. However, camera vignetting occurs only on the part of the intra-focal chips located further away from the center (see Figure 2). It is also solely a function of distance from the center of the field. One way to limit the impact of vignetting is to limit the selection of the donuts to the ones within a certain distance from the center of the focal plane, when possible. Figure 6 shows the impact of the vignetting on the measurement accuracy. We

*https://github.com/LSSTDESC/imSim

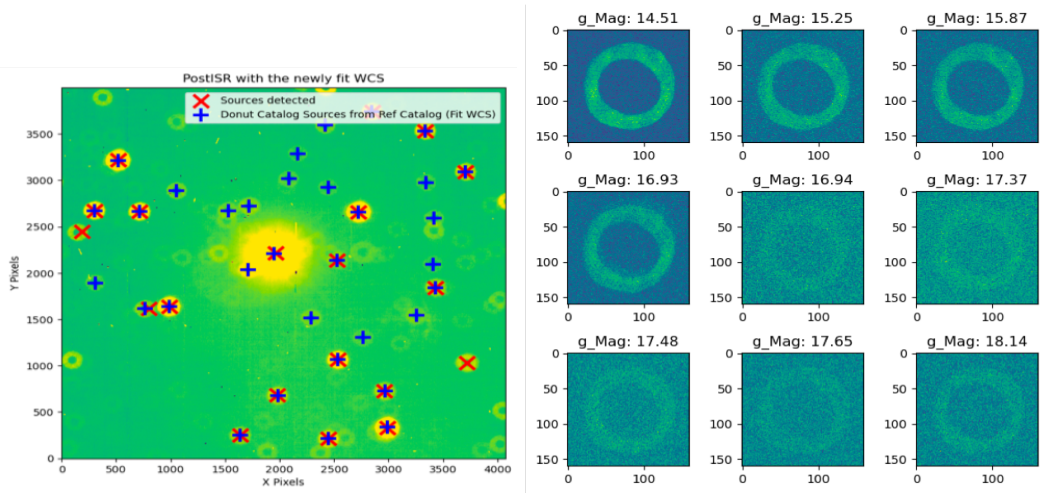


Figure 5. Left: full image with potential donuts corresponding to the selected donuts based on the following criteria: magnitude of the targets, field position of the targets (for vignetting), separation from neighboring sources, magnitude difference between neighbors, number of blended neighbors, and amount of overlap of blended neighbors (for validity of deblending algorithm). Right: example of donuts samples as a function of magnitude.

found that closed-loop for vignetted sources converges with the same (unvignetted) accuracy up to 1.813 degrees from center, which only rules out 5% of the intra-focal sensor area.

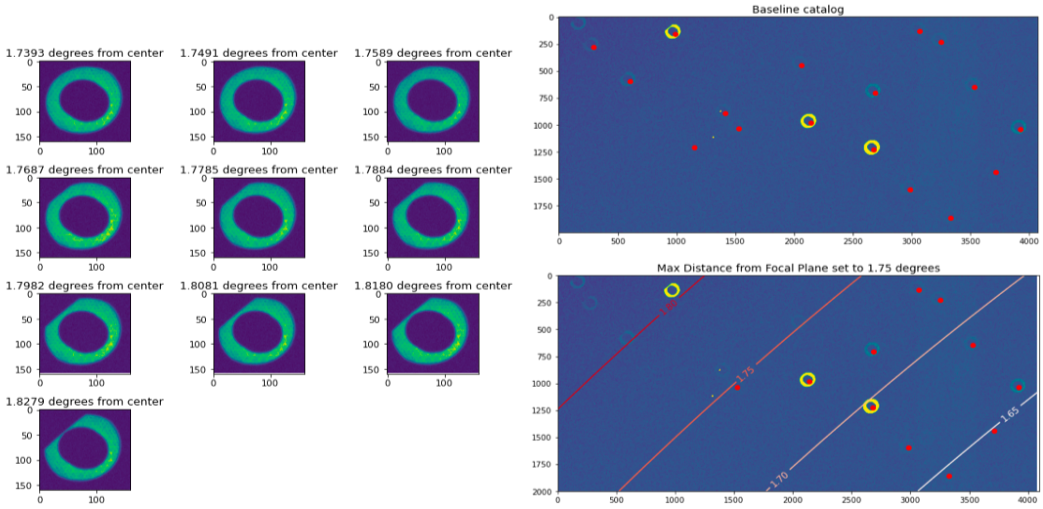


Figure 6. Vignetting. Left: example of vignetted donuts located at different distances from the center of the focal plane. Right: selection examples. The top figure shows were the detections (red dots) without using a selection criteria on the vignetting ratio and the bottom shows the same image but with a selection criteria for the sources located within 1.75deg of the center of the focal plane.

The same methodology is used to understand how much overlap of sources, or blending, is allowed. Indeed, when two donuts are overlapping, we can mask the overlap region and still use the same method as if it were vignetted. We show that this deblending method was applicable with 30% overlap. It is computationally fast and allow a sky coverage of 93% in r band. Part of the planned optimization for the upcoming year is the implementation of more sophisticated methods that would increase sky coverage.

## 2. OPTICAL FEEDBACK CONTROLLER

The optical feedback controller calculates the force offsets that need to be applied to the mirror actuators and positions that need to be applied to the hexapods, from the wavefront estimate. The optical feedback controller is composed of an optical state estimator and a Linear Quadratic Gaussian controller [15]. The optical state estimator calculates the state of the system, namely the residual mirror deformations present in the M1M3 and the M2 planes, as well as the misalignments of M2 and the camera relative to M1M3, after correction. It does so by inverting the sensitivity matrix, which is the response matrix that relates the optical state in the basis of degrees of freedom to the wavefront Zernike coefficients at different field points (either the four wavefront sensors or the 189 science detectors).

The sensitivity matrix is highly degenerate, meaning that different applied degrees of freedom have the same effect. In the presence of noise, this near-degeneracy affects the optical state estimation resulting in incorrectly estimating degenerate perturbations, leading to noise propagation. Different approaches to deal with the degeneracy, both in the optical state estimation and the controller, are currently under investigation and will need to be tested during commissioning.

While the basic algorithm [1, 14] has been functional and tested for fixed rotations for a while, it failed to address the rotation of the camera with respect to the other optical elements of the telescope. However, during normal operation of the telescope, the camera will rotate to compensate for sky rotation.

To deal with this camera rotation, we employ a Double Zernike formalism that encodes the variation of each Zernike coefficient across the pupil as a Zernike expansion across the field of view [5, 10]. This allows us to account for the variation of the wavefront across the field and across the pupil at the same time. Equations 1 and 2, respectively show the formalism for the wavefront variation $W(u)$ across pupil at single field point $u$ and the variation of expansion coefficients $a_j(\theta)$ of $W(u)$ over the field $\theta$.

$$W(u,\theta) = \sum_j a_j(\theta) Z_j(u) \tag{1}$$

$$a_j(\theta) = \sum_k b_{jk} Z_k(\theta) \tag{2}$$

where $Z_j$ is the Zernike polynomial and $b_{jk}$ is the Zernike coefficient of the double expansion.

The Double Zernike representation enables us to evaluate the pupil wavefront at arbitrary positions within the field-of-view, which is required when the camera rotator moves the wavefront sensors into new positions. Since the wavefront sensors also rotate when the camera rotator engages, we also take advantage of the possibility to analytically manipulate Zernike coefficients under coordinate system rotations [10]. The Double Zernike representation, with analytic rotations, is used both for the reference wavefront of the telescope and the sensitivity matrix.

The second component of the optical feedback controller is the Linear Quadratic Gaussian controller. It derives the corrections to be applied to the mirror bending modes and the corrected hexapod positions. It computes these corrections by balancing two driving objectives, the minimization of the wavefront error over 30 Gaussian quadrature points, and the avoidance of large swings and degenerate modes in the derived corrections. With these two complementary objectives, the cost function can be expressed in two terms as,

$$J = \sum_i w_i ||\vec{y_i}||_Q^2 + \rho ||\vec{u}||_H^2 \tag{3}$$

where $y_i$ is the wavefront error at Gaussian Quadrature point $i$, $w_i$ is the corresponding weight, $Q$ is the image quality matrix, $u$ are the corrections to be applied, $\rho$ is the motion penalty scalar and $H$ is the penalty matrix. In particular, the penalty matrix allows us to deal with degeneracy in the presence of noise and to distribute the correction over the different degrees of freedom in an a priori way. The optimization of this penalty matrix is currently under investigation, as it will be an important part of commissioning and will likely depend on the noise level.

## 3. DEEP LEARNING APPROACHES

A deep learning system for wavefront estimation has been developed as a complement to the baseline method currently used by the active optics pipeline. These methods were pioneered in [11] and [16]. The Rubin system uses a convolutional neural network based on ResNet-18 [3] to extract salient features from a donut image, and then combines those features with information about the donut position and observation wavelength to predict the annular Zernike expansion of the wavefront on the pupil. This system has been trained and tested on simulated Rubin data, and integrated into the active optics pipeline.

Compared to the baseline wavefront estimation method, the deep learning system is (i) 40x times faster at estimating the wavefront for an individual donut, (ii) the median wavefront estimation error is a factor 2 lower under ideal conditions, (iii) a factor of 5 better in the presence of vignetting by the Rubin camera (Fig. 7, top row), and (iv) a factor of 14 better in the presence of blending in crowded fields (Fig. 7, bottom row). These features indicate that the deep learning system will lead to a quicker, more robust active optics system that will expand the survey area useful for precision science, i.e. with an optimized resolution and signal to noise ratio, by up to 8%. The result is an increase of contingency in the survey overall over the 10 years.

Domain adaptation and transfer learning using commissioning data will likely be required to reach optimal performance using this system with real data from the telescope. A pilot study on this process is being conducted using the Rubin Observatory's Auxiliary Telescope. In the future, we will investigate following the approach of [16] in using a deep learning system to bypass the wavefront and directly predict the optical state of the telescope from the donut images themselves.

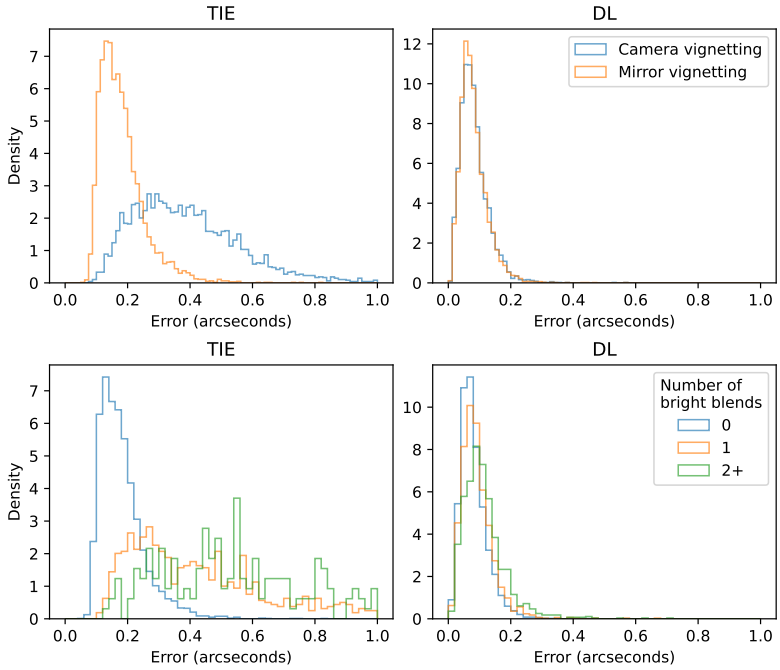


Figure 7. Comparing the performance of the baseline wavefront estimation algorithm (left column, labeled TIE for Transport of Intensity Equation) with the deep learning estimator (right column, labeled DL), in suboptimal conditions. Each histogram is the distribution of wavefront estimation errors for a test set of donuts, where the error is quantified by the increase in the telescope's PSF FWHM due to the misestimation of the wavefront. Top row: performance as a function of vignetting type. All donuts on the wavefront sensors are vignetted by the mirrors, but donuts near the far corners of these sensors are more dramatically vignetted by the camera body. This vignetting degrades the performance of the baseline algorithm, while the deep learning system is robust. Bottom row: performance as a function of the number of bright blends. Here bright means the overlapping source is within 2 magnitudes of the central source. Bright blending significantly degrades the performance of the baseline algorithm, while the deep learning system is robust.

## 4. TOWARDS COMMISSIONING

As the project is getting closer to being on sky, the active optics team is making tremendous progress in finalizing the test plan as well as writing and testing the associated scripts. The AOS control software has been fully integrated and tested with real components; the mirror systems with their surrogate, the Commissioning Camera (ComCam), the hexapods, the rotator, the control software and other components of the Observatory Control Software. The team is now detailing the on-sky plan that will focus first on aligning the telescope and its camera (including hunting for sign and rotation errors), then validating our wavefront sensing and optical state estimation and finally optimizing the parameters of the control system (see Figure 8).

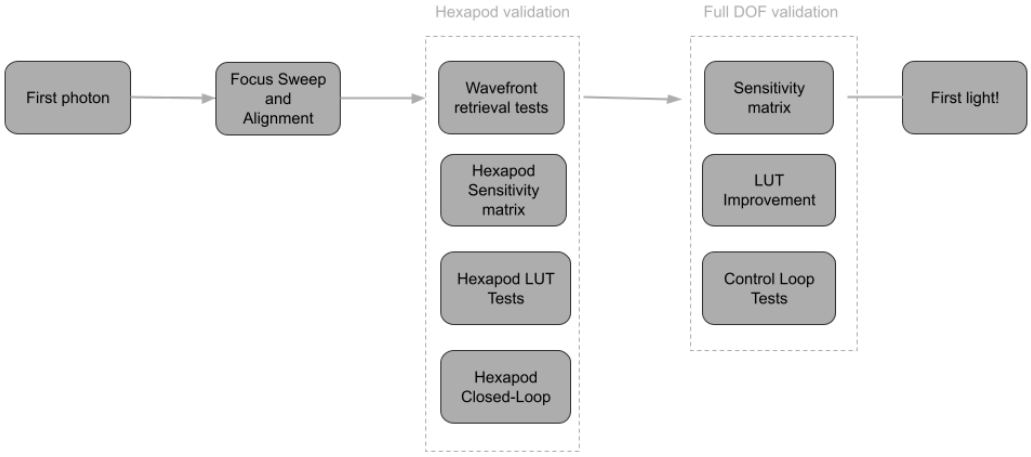


Figure 8. Steps of the on sky testing

The first part of on-sky testing will focus on the alignment of the telescope and the LSSTCam. Preparation work using the laser tracker mentioned above would have happened, meaning that the remaining on-sky work will mostly be small alignment optimization and focus adjustments. One effective way to align the telescope developed by one of our international contributors is to look at the variation of the PSF first moments across the field of view and from them calculate misalignments. The goal then is to estimate the optical state from the in-focus science image using the PSF moments to measure the aberrations (see Figure 9).

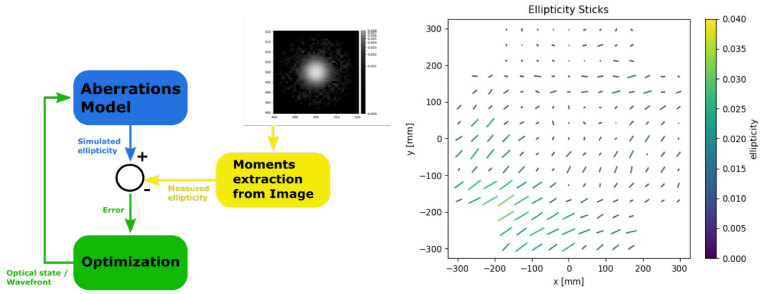


Figure 9. PSF moments method to measurement misalignment and wavefront errors.

Looking beyond the alignment, this image quality estimation from in-focus focal plane images is also a sanity check for the Active Optics. It can also provide additional data to optimize the look-up-table.

## 5. CONCLUSION

The development and testing of the Simonyi Survey Telescope overall Active Optics is reaching maturity, including optimization. The focus is now on on-sky performance testing preparation for June 2024. The team is now detailing the on-sky plan that will focus first on aligning the telescope and its camera (including hunting for sign and rotation errors), then validating our wavefront sensing and optical state estimation and finally optimizing the parameters of the control system . The goal is to evaluate the overall AOS performance and achieve the image quality required over the 3.5 degrees field of view. In addition to preparing the plan, the team is focusing on tools that will help us to more efficiently achieve our goals, including display, image prediction simulation tools, data analysis processes, etc. In parallel, we will continue to explore the very promising technique of machine learning, that has lots of potential to further increase the efficiency of both on-sky testing and operation.

## ACKNOWLEDGMENTS

This material is based upon work supported by the National Science Foundation under Cooperative Agreement 1258333 managed by the Association of Universities for Research in Astronomy (AURA), and the Department of Energy under Contract No. DE-AC02-76SF00515 with the SLAC National Accelerator Laboratory. Additional funding for Rubin Observatory comes from private donations, grants to universities, and in-kind support from LSSTC Institutional Members. The authors would also like to thank Chris Walter for his thorough review of the manuscript.

## References

[1] George Z. Angeli et al. "Real Time Wavefront Control System for the Large Synoptic Survey Telescope (LSST)". In: *Modeling, Systems Engineering, and Project Management for Astronomy VI*. Vol. 9150. SPIE, Aug. 2014, pp. 159–174. DOI: 10.1117/12.2055390. URL: https://www.spiedigitallibrary.org/conference-proceedings-of-spie/9150/91500H/Real-time-wavefront-control-system-for-the-Large-Synoptic-Survey/10.1117/12.2055390.full (visited on 01/10/2023).

[2] F. et al. Daruich. "Rubin Observatory Primary Tertiary Mirror Cell Assembly: Integration and Functional Tests". In: vol. 9150. Society of Photo-Optical Instrumentation Engineers (SPIE) Conference Series. Dec. 2020.

[3] Kaiming He et al. "Deep Residual Learning for Image Recognition". In: *2016 IEEE Conference on Computer Vision and Pattern Recognition, CVPR 2016, Las Vegas, NV, USA, June 27-30, 2016*. IEEE Computer Society, 2016, pp. 770–778. DOI: 10.1109/CVPR.2016.90. URL: https://doi.org/10.1109/CVPR.2016.90.

[4] Željko Ivezić et al. "LSST: From Science Drivers to Reference Design and Anticipated Data Products". In: *The Astrophysical Journal* 873 (Mar. 2019), p. 111. DOI: 10.3847/1538-4357/ab042c. URL: http://adsabs.harvard.edu/abs/2019ApJ...873..111I (visited on 09/13/2020).

[5] Ivo W Kwee and Joseph J M Braat. "Double Zernike expansion of the optical aberration function". In: *Pure and Applied Optics: Journal of the European Optical Society Part A* 2.1 (Jan. 1993), p. 21. DOI: 10.1088/0963-9659/2/1/004. URL: https://dx.doi.org/10.1088/0963-9659/2/1/004.

[6] LSST Dark Energy Science Collaboration (LSST DESC) et al. "The LSST DESC DC2 Simulated Sky Survey". In: 253.1, 31 (Mar. 2021), p. 31. DOI: 10.3847/1538-4365/abd62c. arXiv: 2010.05926 [astro-ph.IM].

[7] D. R. Neill et al. "LSST secondary mirror system final design". In: *Ground-based and Airborne Telescopes VI*. Vol. 9906. Proc. SPIE. July 2016, 990667, p. 990667. DOI: 10.1117/12.2234021.

[8] J. R. Peterson et al. "Simulation of Astronomical Images from Optical Survey Telescopes Using a Comprehensive Photon Monte Carlo Approach". In: 218.1, 14 (May 2015), p. 14. DOI: 10.1088/0067-0049/218/1/14. arXiv: 1504.06570 [astro-ph.IM].

[9] C. Roddier and F. Roddier. "Wave-Front Reconstruction from Defocused Images and the Testing of Ground-Based Optical Telescopes." In: *Journal of the Optical Society of America A* 10 (Nov. 1993), pp. 2277–2287. DOI: 10.1364/JOSAA.10.002277. URL: https://ui.adsabs.harvard.edu/abs/1993JOSAA..10.2277R (visited on 07/19/2023).

[10] Eric Tatulli. "Transformation of Zernike coefficients: a Fourier-based method for scaled, translated, and rotated wavefront apertures". In: *Journal of the Optical Society of America A* 30.4 (Apr. 2013), p. 726. DOI: 10.1364/JOSAA.30.000726. arXiv: 1302.7106 [astro-ph.IM].

[11] David Thomas, Joshua Meyers, and Steven M. Kahn. "Improving Astronomy Image Quality Through Real-Time Wavefront Estimation". In: *Proceedings of the IEEE/CVF Conference on Computer Vision and Pattern Recognition (CVPR) Workshops*. June 2021, pp. 2076–2085.

[12] Sandrine J. Thomas et al. "Rubin Observatory active optics system status". In: *Society of Photo-Optical Instrumentation Engineers (SPIE) Conference Series*. Vol. 11445. Society of Photo-Optical Instrumentation Engineers (SPIE) Conference Series. Dec. 2020, 114452D, p. 114452D. DOI: 10.1117/12.2561094.

[13] Sandrine J. Thomas et al. "Rubin Observatory Simonyi Survey Telescope Status Overview". In: 12182 (Aug. 2022), 121820W. DOI: 10.1117/12.2630226. URL: https://ui.adsabs.harvard.edu/abs/2022SPIE12182E..0WT (visited on 07/13/2023).

[14] Sandrine J. Thomas et al. "The LSST Real-Time Active Optics System". In: *AO4ELT5 Proceedings*. Tenerife, Canary Islands, Spain: Instituto de Astrofísica de Canarias, June 2017. DOI: 10.26698/AO4ELT5.0137.

[15] Bo Xin et al. "Curvature Wavefront Sensing for the Large Synoptic Survey Telescope". In: *Applied Optics* 54 (Oct. 2015), p. 9045. ISSN: 0003-6935. DOI: 10.1364/AO.54.009045. (Visited on 09/09/2022).

[16] Jun E. Yin et al. "Active Optical Control with Machine Learning: A Proof of Concept for the Vera C. Rubin Observatory". In: *AJ* 161.5 (Apr. 2021), p. 216. ISSN: 1538-3881. DOI: 10.3847/1538-3881/abe9b9. URL: https://doi.org/10.3847/1538-3881/abe9b9 (visited on 11/04/2021).